Many-particles–plus–rotor description of magnetic bands at high spin

B. G. Carlsson and I. Ragnarsson
Division of Mathematical Physics, LTH, Lund University. P.O. Box 118, SE-221 00 Lund, Sweden
(Received 9 June 2006; published 25 October 2006)

The high-spin parts of shears bands observed in ^{198,199}Pb are described by coupling several valence particles to a deformed rotor core. To give the model enough freedom so that both the proton and the neutron spin vectors can find their preferred direction, the use of five to six valence particles and holes is found to be necessary. Effective parameters characterizing the rotor are deduced from the cranking model. The method is described and results are presented concerning transition probabilities and energies in the high-spin regime for several rotational bands in ^{199}Pb. The possible termination of the rotational bands is also discussed.

DOI: 10.1103/PhysRevC.74.044310 PACS number(s): 21.10.Re, 21.60.Ev, 21.10.Ky, 27.80.+w

I. INTRODUCTION

Magnetic rotation [1] has been labeled a new mode of excitation that differs from well-known excitation modes. It occurs for relatively small deformations but gives rise to regular sequences of states interpreted as the result of a gradual alignment of two originally perpendicular angular momentum vectors. The magnetic bands observed in the lead region have been described as two protons preferring to align their angular momenta with one axis and a couple of neutron holes that align their angular momentum vector with a perpendicular axis (see Refs. [1,2]). This coupling creates a large magnetic moment perpendicular to the direction of the total nuclear spin that gives rise to large magnetic dipole transitions. Spin increases as the two spin vectors align, which creates a smaller magnetic moment and a characteristic decrease of the magnetic dipole transitions with increasing angular momentum. Because the total angular momentum increases mainly due to the alignment of two spin vectors, this mode of excitation has been labeled the shears mechanism [3]. A special feature of the shears mechanism is that the nuclear spin axis remains at an essentially fixed angle when the spin increases. This requires that both the high-j protons and the high-j neutron holes have the freedom to build angular momentum both along the symmetry axis and along the perpendicular axis.

As the magnetic bands reach the maximum spin that can be built by the alignment, there is the question whether the bands terminate [4,5], i.e., reach their end in an axially symmetric state with the angular momentum pointing in the direction of a symmetry axis of the potential in which case it is not possible to build higher angular momenta within that configuration. Such a termination would give rise to a decrease of the electric quadrupole transitions, reflecting the changes in deformation of the average nuclear field together with the reorientation of the angular momentum vector. As an alternative to termination it is also possible that couplings with states outside the valence space are strong enough to generate higher spin states in a collective manner in which case there would be no drastic reduction of the electric quadrupole transitions [6].

The present work aims at gaining an increased insight into the magnetic bands in the lead region while evaluating an alternative model. Previous theoretical descriptions have relied on the tilted axis cranking model (TAC) [1,7,8], which has been successful in describing the observed large magnetic dipole transitions [2]. In this model the energy is minimized with respect to the orientation of the cranking vector and semi-classical formulas are used to calculate transition probabilities within rotational bands.

In the alternative approach presented here, the cranking model is used for the bulk of the nucleons, with several valence particles coupled to the bulk using the particle rotor model (PRM [9]). This approach yields wave functions in the laboratory frame having good total spin. From these wave functions, transition probabilities can be calculated not only within bands but also between bands and rotational bands can be followed as they cross the boundary from the tilted regime to the principal axis cranking regime. The method involves a core that has to be treated as a macroscopic rotor. Furthermore, it relies on the possibility to find a proper division between the core and particle spaces.

The basic features of the model are discussed in Sec. II. Our method to extract the properties of the rotor are described in Sec. III, followed by a comparison with principal axis cranking (PAC), a discussion of how the shell correction method can be introduced and a comparison between results obtained for different divisions between the particle space and the core space. Different configurations of ^{199}Pb are discussed in some detail in Sec. IV and compared with experiment. Finally, in Sec. V, the importance of allowing the neutron spin vector tilt away from the perpendicular axis is demonstrated. In this first article we concern ourselves only with the high-spin part of the bands and discuss the evidence for an oblate to prolate shape transition at high spin.

II. MODEL

The model presented here is based on single-particle orbitals in a deformed potential in a similar way as the two-quasiparticle plus rotor model of Ref. [10]. Compared with Ref. [10], it is formulated for an arbitrary number of (quasi-)particles but with the drawback that pairing is neglected at present. It is illustrative to compare with the model of Ref. [11], where also an arbitrary number of quasiparticles is included but where the particle space is limited to a pure j shell. Although the present model is formulated for triaxial shapes, we have confined ourselves to axial symmetric shapes

in the numerical calculations presented here. The Hamiltonian can be written (cf. Refs. [10,12])

$$\begin{aligned} H &= H_{\rm rot} + h_{\rm s.p.} = E_0^{\rm rot} + \sum_{k=1}^{3} \frac{R_k^2}{2\mathcal{J}_k} + h_{\rm s.p.} \\ &= E_0^{\rm rot} + \sum_{k=1}^{3} \frac{(I_k - j_k)^2}{2\mathcal{J}_k} + h_{\rm s.p.} \\ &= \frac{1}{2}\left(\frac{1}{2\mathcal{J}_1} + \frac{1}{2\mathcal{J}_2}\right)\left[(I^2 - I_3^2) + (j^2 - j_3^2)\right. \\ &\quad \left. - (I_+ j_- + I_- j_+)\right] + \frac{1}{4}\left(\frac{1}{2\mathcal{J}_1} - \frac{1}{2\mathcal{J}_2}\right)[(I_+^2 + I_-^2) \\ &\quad + (j_+^2 + j_-^2) - 2(I_+ j_+ + I_- j_-)] \\ &\quad + \frac{(I_3 - j_3)^2}{2\mathcal{J}_3} + \sum_i e_i a_i^\dagger a_i + E_0^{\rm rot} + h_{\rm s.p.}, \end{aligned} \tag{1}$$

where $h_{\rm s.p.}$ is a deformed single-particle Hamiltonian and $H_{\rm rot}(\mathcal{J}_1, \mathcal{J}_2, \mathcal{J}_3)$ is the particle-rotor Hamiltonian [9]. A constant $E_0^{\rm rot}$ has been added that represents the energy of the rotor at spin zero. The indices 1,2,3 refer to the body-fixed frame, where we will use the 3 axis as the symmetry axis in the case of axial symmetry ($\mathcal{J}_1 = \mathcal{J}_2$). The energy is minimized with respect to deformation and the moments of inertia for the core are determined using cranking calculations as will be discussed below. Thus the only free parameters enter in the description of the mean-field potential where we have employed the modified oscillator using the so-called standard parameters [13] and with the shape of the potential parameterized using the $(\varepsilon_2, \gamma, \varepsilon_4)$ parametrization. In the present code, the pairing correlations are not taken into account. Indeed, without pairing it is much more straightforward to formulate a consistent formalism. However, pairing should be included for a precise description of the properties in the low-spin region while it should be a good approximation to neglect pairing for the high-spin states considered here.

The diagonalization of $h_{\rm s.p.}(\varepsilon_2, \gamma, \varepsilon_4)$ leads to single-particle states written as expansions [12]

$$a_{t_z,v}^\dagger |0\rangle = \sum_{Nj\Omega} c_{Nlj\Omega}^{(v)} |Nlj\Omega\rangle$$

with Ω restricted to $\ldots, -3/2, 1/2, 5/2, \ldots$ and thus signature [14] $\alpha_i = 1/2$. The conjugate orbitals with signature $\alpha_i = -1/2$ can be defined as (see Appendix A)

$$\begin{aligned} a_{t_z,\widetilde{v}}^\dagger |0\rangle &= e^{-i\pi j_2} a_{t_z,v}^\dagger e^{i\pi j_2} |0\rangle \\ &= \sum_{Nj\Omega} (-1)^{j-\Omega} c_{Nlj\Omega}^{(v)} |Nlj - \Omega\rangle . \end{aligned}$$

If only protons are written explicitly the wave function $|\alpha\rangle$ describing the particle space is defined as

$$|\alpha\rangle = \left(\prod_{i=1}^{z_1} a_{1/2,\beta_i}^\dagger\right)\left(\prod_{i=1}^{z_2} a_{1/2,\widetilde{\gamma}_i}^\dagger\right)|0\rangle .$$

Each creation operator is labeled using two quantum numbers. They specify the isospin (proton, 1/2 and neutron, $-1/2$) and the signature of the particle, where the second number is also used to specify the ordering of the states within the symmetry group. The rotated basis functions $|\widetilde{\alpha}\rangle$ can be written

$$|\widetilde{\alpha}\rangle = (-1)^{z_2}(-1)^{z_1 z_2}\left(\prod_{i=1}^{z_2} a_{1/2,\gamma_i}^\dagger\right)\left(\prod_{i=1}^{z_1} a_{1/2,\widetilde{\beta}_i}^\dagger\right)|0\rangle ,$$

where the first phase factor is a minus sign for each particle rotated a full revolution and the second one comes from permuting the order so that signature 1/2 states comes first. The total wave function is thus divided into four different groups consisting of signature $\alpha_i = \pm 1/2$ protons and neutrons, which is convenient when calculating matrix elements. The number of neutrons and protons of a certain parity are preserved quantum numbers in the model.

The total Hamiltonian H is diagonalized in the coupled and symmetrized basis [9]

$$\begin{aligned} \left|\Psi_{MK\alpha}^I\right\rangle &= N_{\alpha K}\frac{1}{\sqrt{2}}(1 + e^{-ij_2\pi}e^{iI_2\pi})\sqrt{\frac{2I+1}{8\pi^2}}|IMK\rangle|\alpha\rangle \\ &= N_{\alpha K}\sqrt{\frac{2I+1}{16\pi^2}}(|IMK\rangle|\alpha\rangle + (-1)^{I-K}|IM-K\rangle|\widetilde{\alpha}\rangle), \end{aligned} \tag{2}$$

where $|IMK\rangle$ denotes the usual rotation matrix. The normalization constant $N_{\alpha K}$ is equal to one except when $K = 0$ and the rotated state $|\widetilde{\alpha}\rangle = e^{-ij_2\pi}|\alpha\rangle$ is the same as $|\alpha\rangle$, which happens when an even number of particles are placed in time-reversed orbits. In this case a different normalization is required, $N_{\alpha K} = 1/\sqrt{2}$.

In the axially symmetric case the basis states can be labeled with their projections on the symmetry axis $k = k_p + k_n$, where k_p and k_n are the sums of the single-particle projections Ω for protons and neutrons, respectively. In this case the core is not allowed to build spin in the direction of the symmetry axis (the 3 direction), which leads to the restriction $K = k$. When evaluating the matrix elements of H, the operators in Eq. (1) are written using second quantization as sums of one- and two-body operators (see Appendix B). In the calculation, the configuration space in the different symmetry groups typically consists of 5–10 doubly degenerate orbitals from the deformed single-particle Hamiltonian. Because all possible particle-hole excitations within this space are considered the dimensions are generally quite large for several particles. In these cases the ARPACK routines [15] are used when solving numerically for the lowest eigenvalues and corresponding wave functions.

The formulas for reduced transition probabilities are straightforward to derive, leading to expressions that are similar to those obtained for one particle in Refs. [12,16]. The resulting formula for the $B(E2)$ value is

$$\begin{aligned} B(E2; I_i \to I_f) = \frac{5e^2}{16\pi}\Bigg| &\sum_{K_f,\alpha_f,K_i,\alpha_i} a_{K_f}^{I_f\alpha_f} a_{K_i}^{I_i\alpha_i} N_{\alpha_i K_i} N_{\alpha_f K_f} \\ &\times \left\{ \sum_{\mu=-2,0,2} \left(Q_{2\mu}^{\rm core}\langle\alpha_f|\alpha_i\rangle + \langle\alpha_f|\widehat{q}_{2\mu}|\alpha_i\rangle\right)\right. \\ &\left. \times \langle I_i K_i 2\mu | I_f K_f\rangle + (-1)^{I_i - K_i}\right. \end{aligned}$$

$$\times \left(Q_{2\mu}^{\rm core}\langle\alpha_f|\widetilde{\alpha}_i\rangle + \langle\alpha_f|\widehat{q}_{2\mu}|\widetilde{\alpha}_i\rangle\right)$$
$$\times \langle I_i - K_i 2\mu | I_f K_f\rangle \Bigg\}\Bigg|^2,$$

where the contribution from the core $Q_{2\mu}^{\rm core}$ is added to the diagonal elements. The $B(M1)$ transition probability is obtained as (in units of μ_N^2)

$$B(M1; I_i \to I_f) = \frac{3}{4\pi}\Bigg|\sum_{K_f,\alpha_f,K_i,\alpha_i} a_{K_f}^{I_f\alpha_f} a_{K_i}^{I_i\alpha_i} N_{\alpha_i K_i} N_{\alpha_f K_f}$$
$$\times \Bigg\{\delta_{I_i,I_f} g_R \sqrt{I_f(I_f+1)}(\langle\alpha_f|\alpha_i\rangle\delta_{K_i,K_f}$$
$$+ (-1)^{I_i-K_i}\langle\alpha_f|\widetilde{\alpha}_i\rangle\delta_{K_i,-K_f})$$
$$+ \sum_{\mu=-1,0,1}\langle I_i K_i 1\mu | I_f K_f\rangle\langle\alpha_f|(g_s - g_l)s_\mu$$
$$+ (g_l - g_R)j_\mu|\alpha_i\rangle + (-1)^{I_i-K_i}$$
$$\times \langle I_i - K_i 1\mu | I_f K_f\rangle\langle\alpha_f|(g_s - g_l)s_\mu$$
$$+ (g_l - g_R)j_\mu|\widetilde{\alpha}_i\rangle\Bigg\}\Bigg|^2.$$

Throughout this work we have used $g_s = 0.7 g_s^{\rm free}$ and g_R is obtained from cranking calculations as will be discussed below.

III. METHOD OF CALCULATION

A. Properties of the rotor extracted from cranking calculations

The particle-rotor formalism is based on a division of the relevant degrees of freedom into two parts. The rotor part that is assumed to be an even-even nucleus is given the freedom to build angular momenta in three different directions. The cost of doing so is parametrized in the simplest case by three different moments of inertias. Indeed, with the basis of Eq. (2), this is the only possibility. If, however the basis is recoupled so that R becomes a good quantum number [17], it is possible to use an arbitrary parametrization for the core energies, where the VMI expression [18] is one possibility. Such a recoupling becomes involved with many valence particles but is implemented in the two quasiparticles + rotor code of Ref. [10] and will be used below.

To calculate transition probabilities one needs the effective gyromagnetic moment of the rotor together with the quadrupole moments. Our method consists of extracting these macroscopic parameters of the rotor from a cranking calculation. Once the gross properties of the rotor are obtained one can couple it to several valence particles to obtain the full dynamics of the system. This appears particularly appealing for a description of magnetic bands where the most important physics comes from the orientations of a few valence particles.

The rotor properties are obtained by solving the principal axis cranking (PAC) [14] Hamiltonian

$$H_{\rm PAC} = h_{\rm s.p.}(\varepsilon_2, \gamma, \varepsilon_4) - \omega j_1.$$

From the solutions to $H_{\rm PAC}$ we extract energies, quadrupole moments, and gyromagnetic moments. In this work we have considered axially symmetric deformations only where $\mathcal{J}_3 = 0$ and $\mathcal{J}_1 = \mathcal{J}_2$. To extract this moment of inertia, the energy of the core is calculated as a function of spin. First the cranking frequency is determined from the condition

$$\sqrt{I(I+1)} = J_1 = \sum_i^{A_c}\langle\phi_i^\omega|j_1|\phi_i^\omega\rangle, \tag{3}$$

where ϕ_i^ω are the single-particle eigenfunctions of the cranking Hamiltonian, $H_{\rm PAC}$, and where the summation is carried out over the A_c single-particle states which are occupied in the core. Then the total energy in the laboratory frame is calculated as

$$E_{\rm PAC}(J_1) = \sum_i^{A_c}\langle\phi_i^\omega|h_{\rm sp} + \omega j_1|\phi_i^\omega\rangle$$

(see Ref. [14] for details). To obtain the moment of inertia for the rotor we fit $E_{\rm PAC}(J_1)$ with $J_1^2/2\mathcal{J}_1 + E_0^{\rm rot}$ and use $\mathcal{J}_1$ as the moment of inertia for rotation around the 1 axis.

The effective gyromagnetic factor is obtained as

$$g_R(J_1) = [g_{l,\pi}\langle j_{\pi,1}\rangle + (g_{s,\pi} - g_{l,\pi})\langle S_{\pi,1}\rangle + (g_{s,v})\langle S_{v,1}\rangle]/J_1$$

and the quadrupole moment as the sum of the single-particle moments $Q_{2\mu}^{\rm core}(J_1) = \sum_i^{Z_c} q_{2\mu,i}$. For a well-behaved core, g_R and $Q_{20}^{\rm core}$ are only weakly dependent on J_1 and can thus be approximated by their average values within the appropriate spin interval.

B. Comparison between the particle-rotor and the principal axis cranking model

When comparing PRM calculations with cranking, the energy for the lowest states are often somewhat higher in the PRM. This is illustrated in Fig. 1 and can be understood by considering two limits. When the moment of inertia of the rotor $\mathcal{J}$ becomes large the couplings caused by $H_{\rm rot}$ become small. The wave function for the lowest state will then come close to the Hartree-Fock vacuum obtained by occupying the lowest single-particle states. The corresponding energy is not much higher than the sum of the single-particle energies $E_{\rm s.p.}$. In the other limit when $\mathcal{J}$ becomes small it becomes expensive to use the rotor so the valence particles couple to a good spin and the wave function becomes a sum of several slater determinants with an increased energy.

To illustrate the present method, the result of PRM calculations are compared with cranked Nilsson-Strutinsky (CNS) [4,13] calculations in Fig 2. Panel (a) of Fig. 2 shows the calculated energy for a configuration in $^{158}_{66}{\rm Dy}_{92}$ having no $i_{13/2}$ neutrons at a constant deformation of $\varepsilon_2 = 0.2$ using the CNS model (lines). To be more precise, all orbitals emerging from subshells below the $Z = 50$ and $N = 82$ gaps are filled and in addition the lowest 10 and 6 proton orbitals, respectively, of $d_{5/2}g_{7/2}$ and $h_{11/2}$ character and the lowest 10 neutron orbitals of $h_{9/2}f_{7/2}$ character. This configuration is used as a core in the PRM calculation and the dots indicate the energy of the rotor fitted to this band. As seen a reasonable fit can be obtained with a constant moment of inertia up to

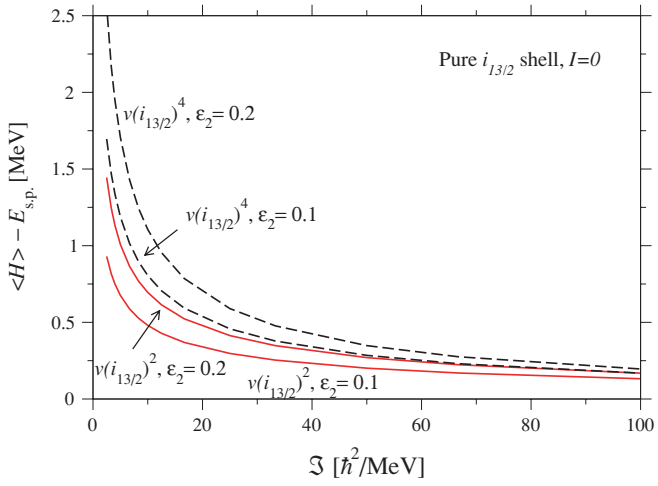

FIG. 1. (Color online) For two and four particles in a pure $i_{13/2}$ shell, the energy calculated in the particle-rotor model for spin $I = 0$ is compared with the single-particle sum, $E_{s.p.}$. As the moment of inertia for the rotor grows, the particles take advantage of the rotor and lower their energy by angular momentum fluctuations. A similar picture illustrating the same effect can be found in Ref. [19].

around spin 35. Using this $^{158}_{66}Dy_{92}$ configuration as a core we couple it to one neutron constrained to 14 orbitals (7 of each signature) originating from the deformed $i_{13/2}$ shell and 10 additional low energy orbitals in the $N = 6$ shell. The result is seen in the panel (b), where it is compared with cranking calculations. The two models produce pretty similar results, the main difference being a somewhat larger signature splitting for the lowest $K = 1/2$ band predicted in the PRM. The difference in the spin alignment between the particle-rotor and cranking model was discussed in Ref. [20], where it was found that the cranking model normally gives a smaller rotation-aligned spin for an odd quasiparticle. The differences were investigated for prolate shapes and found to be largest at low rotational frequencies and with a Fermi level low in the $i_{13/2}$ shell. The explanation for the smaller alignment in the cranking model was found to be the approximation that the average field can be characterized by a constant frequency vector.

In the calculation shown in panel (b) of Fig. 2, the maximum spin contribution from the odd particle is $j_1^{max} = 6.5$ and the PRM results are thus rather dependent on the core properties. However by adding more particles the system becomes less dependent on core parameters. A few more particles can be taken into account explicitly as shown in panels (c) and (d) of Fig. 2. Panel (c) shows the result of coupling four neutrons to the $^{158}_{66}Dy_{92}$ core and panel (d) the results when using five neutrons. With the neutrons confined to an approximately pure $i_{13/2}$ shell, their maximum spin contribution is roughly $j_1^{max} = 20.0$ and 22.5 in the cases of four and five neutrons, respectively, which is a large part of the total spin. The different calculations shown in Fig. 2 use a core with the same numbers of particles. However, the effective single-particle potential for the core is the one valid for the mass number A of the total system of core plus valence particles. Therefore, because of the A dependence of the single-particle potential, the core parameters $\mathcal{J}_i$, Q_{20}, and g_R become slightly different in each case.

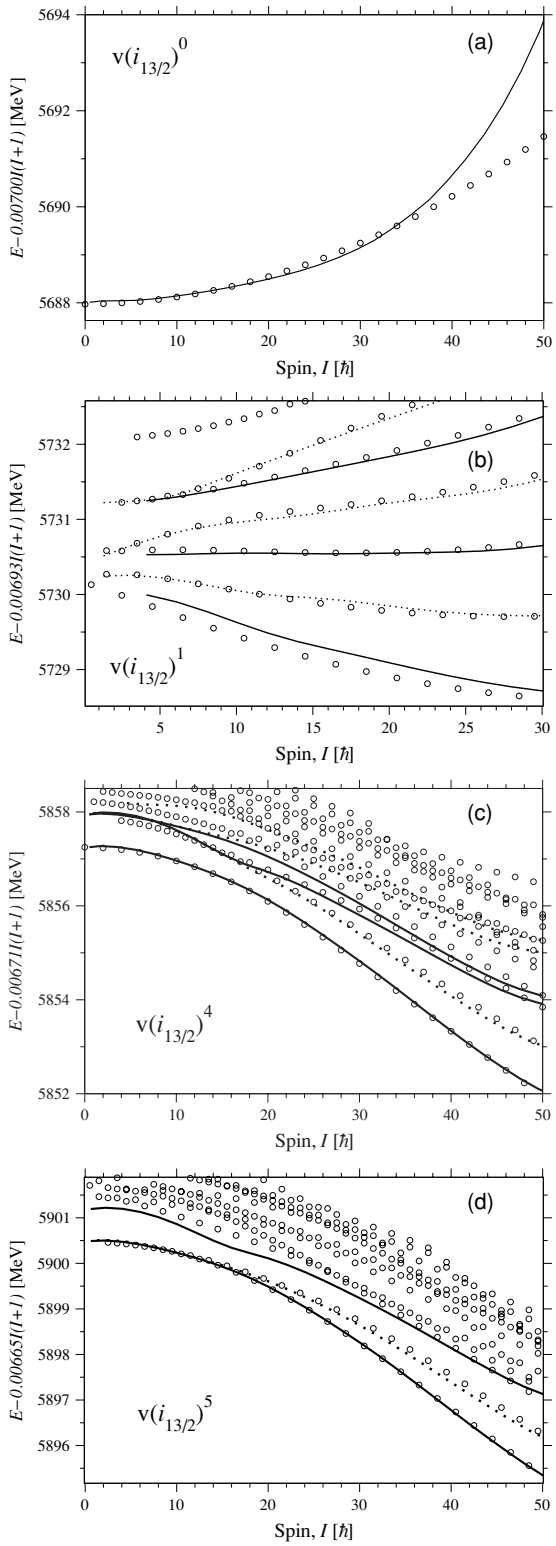

FIG. 2. Comparison of cranking (full and dotted lines) and particle-rotor calculations (circles) for 0,1,4, and 5 $i_{13/2}$ neutrons coupled to a $^{158}_{66}Dy_{92}$ core as defined in the text. Due to the expected energy shift seen in Fig. 1 we have applied constant shifts of the particle-rotor results, placing them so that they roughly agree with the cranking results. Thus, as would be expected from Fig. 1 with $\mathcal{J} \sim 60$, the energies are shifted by 0−0.3 MeV. The deformation is kept constant at $\varepsilon_2 = 0.2$.

In the calculations shown in Fig. 2 the CNS and the PRM give similar results for the energies. In such cases the main advantage of using the more computational demanding PRM is the possibility to calculate transition probabilities between all states.

C. The shell correction method

In Fig. 2 the total energy was obtained as the sum of the single-particle energies counting from the bottom of the modified oscillator potential. When comparing with experiments, the energy is usually Strutinsky renormalized [21] to the average behavior of a liquid-drop model. In a similar way, the smooth part of the rotational energy differs from the experimental energy. Therefore, one usually performs a Strutinsky renormalization also as a function of spin and replaces the average cost of rotating with the energy of a rotating rigid body. This is particularly necessary when using the modified oscillator because the average moment of inertia is roughly 30% larger than the rigid body value [22]. This correction is usually referred to as renormalizing the average moment of inertia and appears to be a quite reliable calculation scheme. In the CNS calculations, the total energy is therefore calculated as [4],

$$E_{\rm tot}(\epsilon_2,\epsilon_4,\gamma,J_1) = E_{\rm PAC}(\epsilon_2,\epsilon_4,\gamma,J_1) - E_{\rm strut}(\epsilon_2,\epsilon_4,\gamma,J_1) + E_{\rm LD}(\epsilon_2,\epsilon_4,\gamma) + \frac{J_1^2}{2\mathcal{J}_1^{\rm rigid}}, \quad (4)$$

where J_1 is defined in Eq. (3). The smoothed single-particle energy sum $E_{\rm strut}(\epsilon_2,\epsilon_4,\gamma,J_1) = \sum \widetilde{e}_i(\widetilde{\omega}_1,\epsilon_2,\epsilon_4,\gamma)|_{\widetilde{J}_1=J_1}$ is calculated using the Strutinsky procedure. $E_{\rm strut}$ thus represent the average energy when the shell structure is smeared out. In this way one can reproduce the local variations which the single-particle potential is fitted to and replace the average behavior with a rotating liquid-drop model. The smoothed cost is calculated for each deformation only along the yrast line and for each value of the spin J_1, the same correction is then applied to all calculated states. The rotating liquid drop energy, i.e., the last two terms in Eq. (4) is described in Ref. [23] and consists of using the LSD model [24] for the static liquid-drop energy with the average moment of inertia $\mathcal{J}_1^{\rm rigid}$ calculated from a mass distribution with a diffuse surface.

We expect the same problem of the smooth part of the energy differing from experiment when using the PRM together with the modified oscillator potential. However, in this case it is difficult to calculate a Strutinsky average as a function of angular momentum. Because the energies obtained in CNS and the PRM are similar, it seems reasonable as a first approximation to apply the same correction also in the PRM, i.e., to add the last three terms of Eq. (4) taken from a CNS calculation to the energy calculated in the PRM. It should be noted that this procedure does not affect the wave functions, reduced transition probabilities, or spin orientation, which is the main interest of this work. The correction makes the average moment of inertia roughly 30% smaller and allows us to compare our results for the energies with renormalized CNS calculations.

D. The division between the particle space and core space

The division into a particle and a core space should be made in such a way that the neglected couplings between the valence particles and the core particles are small. To illustrate how different divisions of core and valence spaces can be made, calculations for $^{198}_{82}\mathrm{Pb}_{116}$ were performed. One of the magnetic bands seen in this nucleus (band 3 in [2,25]) has been described as built with one $i_{13/2}$ proton together with one $h_{9/2}$ proton and four $i_{13/2}$ neutron holes at a small oblate deformation (labeled ABCD11 in Ref. [2,25]). At this deformation the proton particles prefer to align their angular momentum with the symmetry axis (3 axis) and the neutron holes with the perpendicular axis. To describe this band using the PRM it is possible to take all high-j particles as valence particles and treat the remaining part as a rotor. Another possibility is to assume that the spin vectors of the neutron holes stay oriented perpendicular to the symmetry axis and treat them as part of the rotor. These two different core choices are illustrated in Fig. 3. When using the small core, the neutron holes are treated as 10 neutron particles in a deformed $i_{13/2}$ shell. The rotor is thus made up from a nucleus having two less protons and 10 less neutrons than $^{198}_{82}\mathrm{Pb}_{116}$, i.e., from a fixed configuration that, relative to a $^{208}_{82}\mathrm{Pb}_{126}$ core, has two $N=4$ proton holes, six $N=5$ neutron holes, and no $i_{13/2}$ neutrons. For the larger core the cost of building spin cannot be parametrized with a

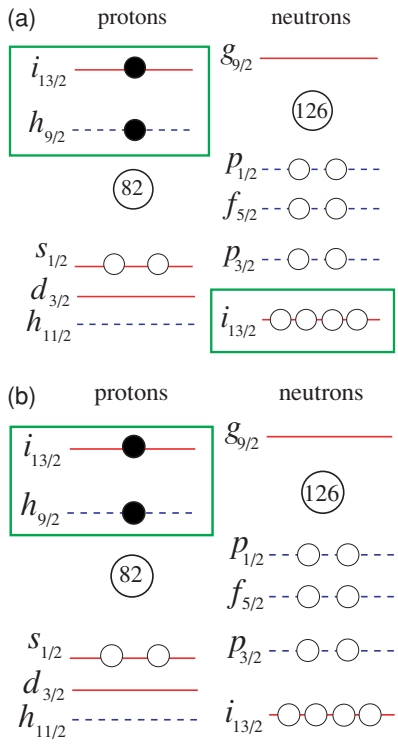

FIG. 3. (Color online) Two different choices of valence spaces for ^{198}Pb. Particles relative to the closed core nucleus ^{208}Pb are shown with filled circles and holes by open circles. The boxes indicate the particles or holes treated explicitly in the particle-rotor calculation. If the core spin is only built from the j shells in this figure, the upper choice of core has a maximum spin of $I_{\rm max}=8$ and the lower one has $I_{\rm max}=28$.

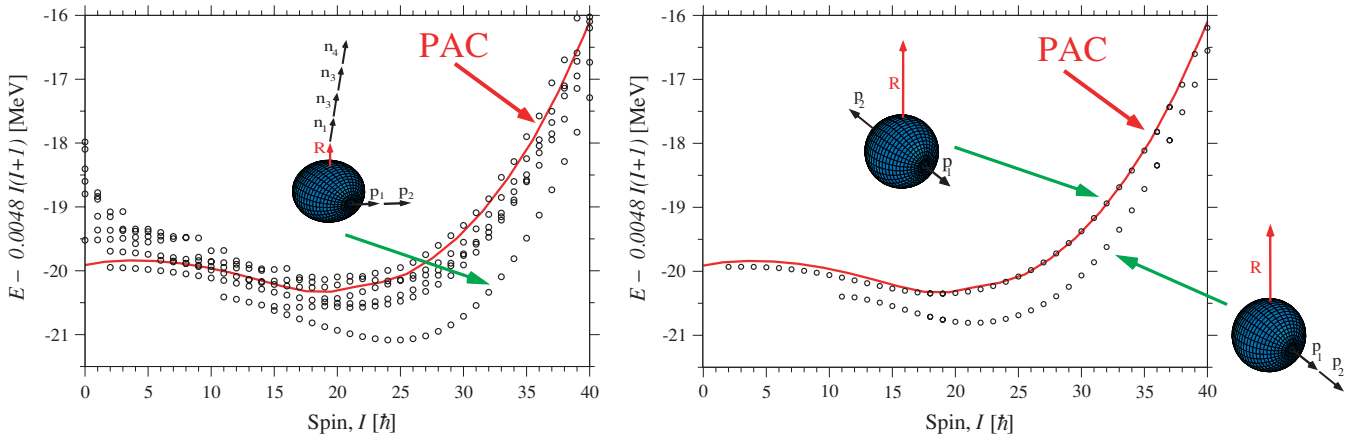

FIG. 4. (Color online) Calculations for ^{198}Pb with a $\pi(i_{13/2})^1(h_{9/2})^1\nu(i_{13/2})^{-4}$ configuration at a constant deformation of $\varepsilon_2 = -0.15$. Left panel shows two protons and four neutron holes coupled to a rotor and in the right panel the neutron holes are treated as part of the core. To be able to compare with PAC calculations the PRM energies has been placed by demanding that the bandhead $I = 2$ states has the expectation value of $h_{\text{s.p.}}$ of the dominating slater determinant in the wave function as their total energy. This means ignoring the correlation energy shown in Fig. 1 and amounts to shifting the PRM energies in left panel by 974 keV and those right panel by 105 keV. Schematic figures illustrate the coupling schemes in the different cases.

constant moment of inertia. The reason is the relatively small rotational energy needed to align the spin of the $i_{13/2}$ neutron holes with the cranking axis. In this case the method mentioned in Sec. III A [17] is used to expand the basis states in a basis where the rotor spin is a good quantum number that can then be used to specify the cost to build each unit of rotor spin. The energy versus spin curves for the calculations using the different choices of cores are shown in Fig. 4 and compared with the result of PAC calculations.

As seen in the right panel, where the neutron holes have been treated as part of the core, the result of the PAC calculation coincides with the first excited PRM band corresponding to an antiparallel coupling of the two protons. This is to be expected since the spin component along the symmetry axis is neglected in PAC calculations. Therefore bands with the parallel and the antiparallel coupling of the protons are degenerate in this model. In the PRM calculation the spin component along the symmetry axis is accounted for which leads to a lowering of the energy compared to the PAC result.

The left panel shows the result when using the larger valence space. In this figure more states have been included. Many of these additional states correspond to excitations among the neutrons. The general features of the magnetic band is, however, the same, whereas the band with the antiparallel coupling of the protons is hard to distinguish. With this small core the dimension of the Hamiltonian becomes rather large, e.g., the basis size is 84084 for both the even- and the odd-signature high-spin states.

Figure 5 shows the calculated transition probabilities for the two different core choices. For both choices the $B(M1)$ values decrease at higher spins, whereas the $B(E2)$ values increase. The trend for the $B(E2)$ values would, however, be

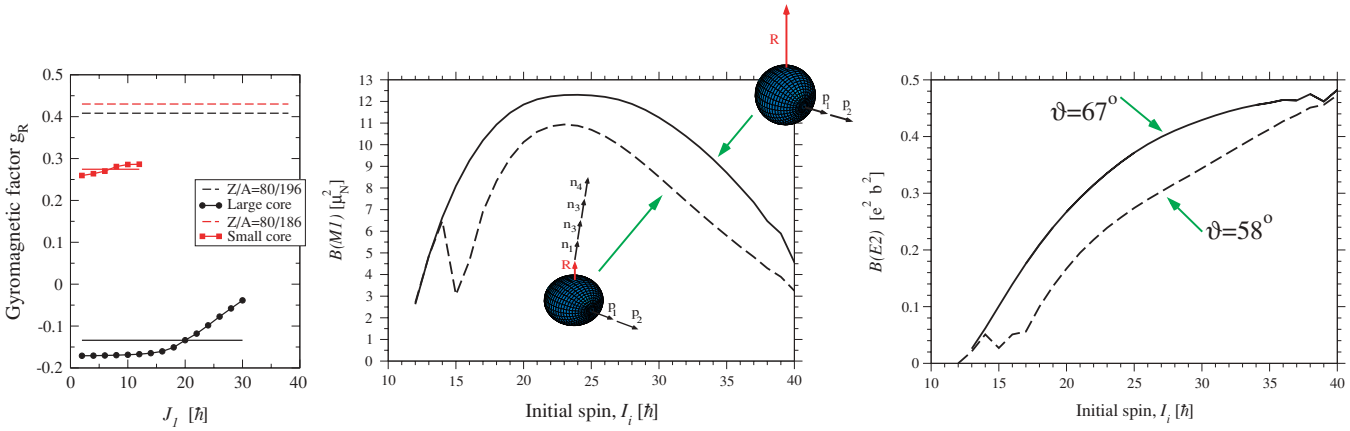

FIG. 5. (Color online) Gyromagnetic factors and transition probabilities for the two choices of cores indicated in Fig. 3. The g_R factors used to calculate the $B(M1)$ transitions are the mean values of those shown in the left panel of the figure. These mean values are also indicated. For the $B(M1)$ (middle panel) and $B(E2)$ (right panel) transition probabilities, dashed lines correspond to the larger valence space and full lines to the smaller one.

somewhat different for the highest spins if the deformation was allowed to change as a function of spin as exemplified for other configurations in Fig. 13 below. The calculation with the smaller core produces smaller values both regarding the $B(E2)$ and $B(M1)$ values. For the smaller core, discontinuities are seen around $I = 15$ both in the $B(E2)$ and $B(M1)$ values indicating a new band starting at $I = 15$. This new band, which mixes with the $K = 11$ band, starts as a $K = 15$ band, where the neutrons contribute with $4\hbar$ at the band head.

The angle the total spin vector makes with the symmetry axis, $\vartheta = \arccos(\sqrt{\langle I_z^2\rangle}/\sqrt{I(I+1)})$, for the $I = 27$ state is indicated in Fig. 5. A larger angle is calculated when the neutrons are treated as part of the core and thus constrained to point in the direction perpendicular to the symmetry axis. This indicates that the neutrons use the freedom gained when treated explicitly to tilt somewhat toward the protons. A smaller tilt angle also leads to smaller $B(E2)$ values according to the approximate relation [2]

$$B(E2) = \frac{15}{128\pi}(eQ_{20})^2 \sin^4\vartheta.$$

Thus, the inclusion of this degree of freedom in the model, i.e., the possibility for the neutrons to tilt toward the symmetry axis, gives a substantial correction to the reduced transition probabilities.

The effective g_R factors obtained from CNS calculations are illustrated as a function of spin in the left part of Fig. 5 for the two choices of core spaces. If the neutron $i_{13/2}$ holes are treated as part of the core, they give a negative contribution to the effective g_R factor that makes the total g_R value negative. The value $g_R = Z/A$, which is sometimes used for g_R [9], is also indicated. As seen from this figure, the parameters describing the core may differ substantially from macroscopic estimates. Another strategy is then to extract parameters like moments of inertia directly from experiments. However, when treating many particles explicitly this may be difficult because the preferred deformation of the core nucleus may be very different from the one for core + valence particles. Therefore, we have chosen to calculate the core parameters microscopicly. With these recipes, the very different divisions between core and particle spaces lead to rather similar results and the remaining differences can to a large extent be understood as being due to restricting the neutrons to point in the direction of a principal axis.

The experimental transition energies are compared with the calculated ones in Fig. 6. A good description of the transition energies are obtained after the backbend at spin $I = 26$. However, because there are no transition probabilities measured when all particles are aligned, no comparison with experimental $B(M1)$ or $B(E2)$ values is possible.

IV. MAGNETIC ROTATION IN ^{199}Pb

In ^{199}Pb transition probabilities have been observed [26] above the backbend which makes it possible to compare with unpaired calculations for these states. In all of our calculations for this nucleus we use the same neutron configuration having three $i_{13/2}$ holes treated explicitly and six additional holes in the $N = 5$ shell with respect to the $N = 126$ closed shell. Thus the model space is chosen as in panel (a) of Fig. 3 but with only three $i_{13/2}$ holes.

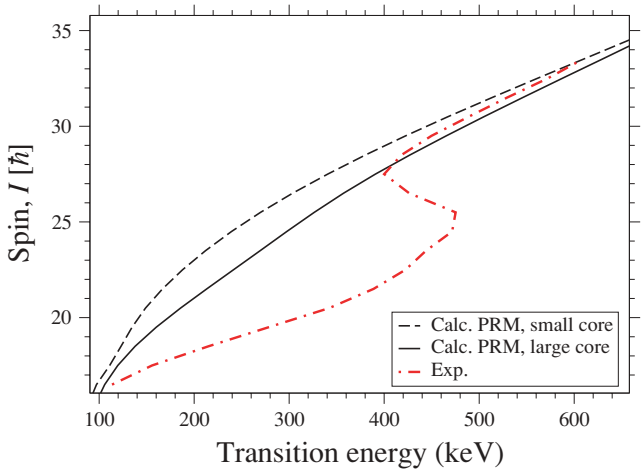

FIG. 6. (Color online) Spin versus transition energy for band 3 in ^{198}Pb and comparison with the calculations in Fig. 4. It is only in the region above the backbend that the experimental moment of inertia becomes close to the unpaired value and where one can expect a quantitative agreement with the PRM calculations.

A. Shapes and possible terminations in ^{199}Pb configurations

Figure 7 shows deformation trajectories for four different proton configurations calculated in the cranked Nilsson-Strutinsky (CNS) formalism. When reaching the maximum spin that can be formed in the valence space, $I_{\max}$, configurations having just one high-j proton show larger tendencies to terminate than those with two high-j protons. For the $\pi(i_{13/2})^1(h_{9/2})^1$ configuration, the two high-j protons can contribute with at most $(13/2 + 9/2)\hbar = 11\hbar$ and the two proton holes with $(3/2 + 1/2)\hbar$ if they are allowed to spread over the $d_{3/2}$ and $s_{1/2}$ subshells. Similarly, the

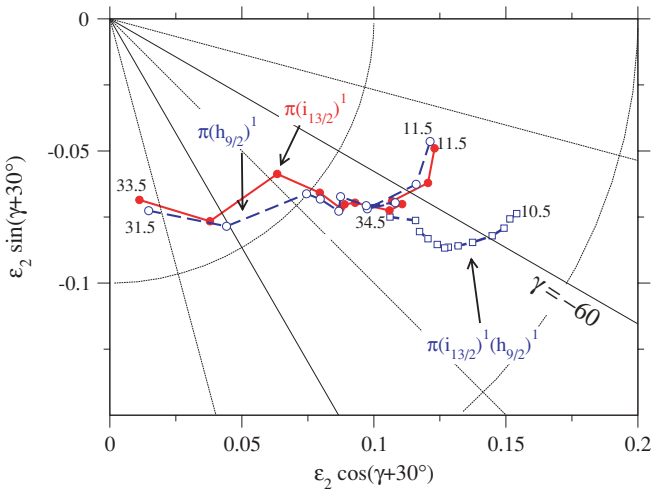

FIG. 7. (Color online) Deformation trajectories calculated using the CNS model. The curves show how the deformation changes as a function of angular momentum in steps of $2\hbar$ for three different configurations.

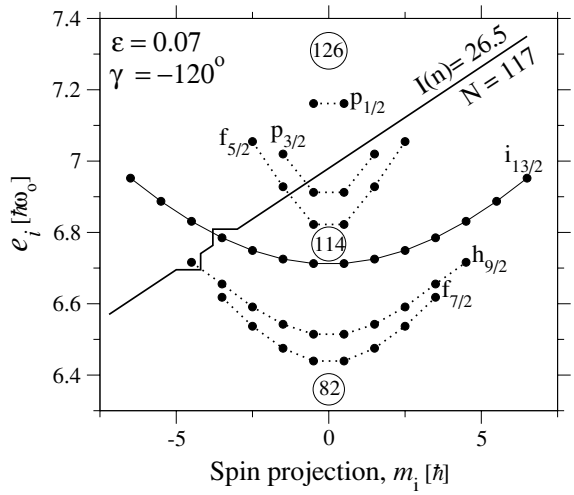

FIG. 8. Tilted Fermi surface plot indicating how the neutron spin is built close to termination. The deformation is the one relevant for the bands with just one high-j proton (see Fig. 7).

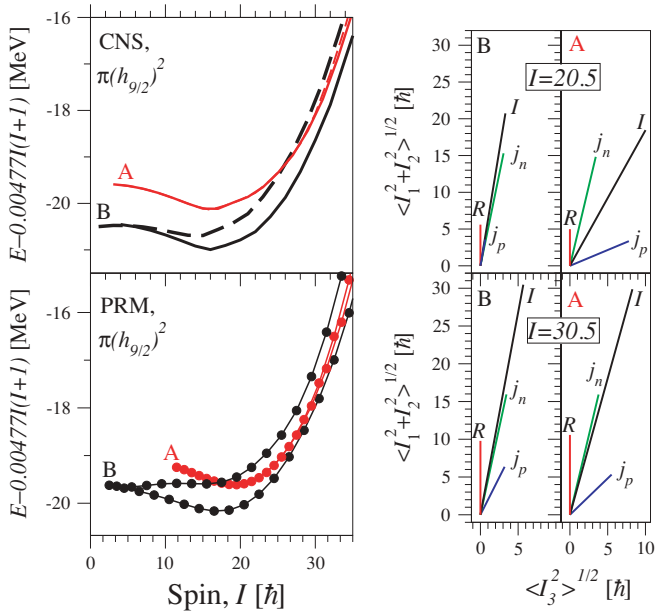

FIG. 9. (Color online) Comparison between PAC (upper left panel) and PRM (lower left panel) for the configuration with 2 $h_{9/2}$ protons. The deformation is kept fixed at $\varepsilon_2 = -0.16$. The orientation of the different spin vectors calculated in the PRM is illustrated at $I = 20.5$ and $I = 30.5$ in the panels to the right.

maximum contribution from the three $i_{13/2}$ neutron holes is $(13/2 + 11/2 + 9/2)\hbar = 16.5\hbar$ and from the six low-j neutron holes $(5/2 + 3/2 + 3/2 + 1/2 + 1/2 - 1/2)\hbar = 6\hbar$ if they are assumed to be equally distributed over the two signatures. We thus arrive at $I_{\max} = 35.5$ for this configuration. The same arguments in the case when the proton configuration has only one high-j proton ($h_{9/2}$ or $i_{13/2}$) leads to $I_{\max} = 28.5$ and 30.5, respectively. However, Fig. 7 shows that these configurations can be followed to higher spins, which is mainly caused by mixing between the $N = 5$ neutron orbitals. Thus these $\pi(h_{9/2})^1$ and $\pi(i_{13/2})^1$ configurations come very close to termination at $I = (31.5^+, 32.5^+)$ and $I = (33.5^-, 34.5^-)$ for the two signatures where the neutron configuration is essentially the one illustrated in a tilted Fermi surface plot in Fig. 8, i.e., with one neutron hole in $h_{9/2}$ so that the maximum neutron spin becomes 26.5 instead of 22.5. For the $\pi(i_{13/2})^1(h_{9/2})^1$ configuration, these couplings (and also the couplings within the $N = 4$ proton holes) become even larger so that the corresponding rotational band can be followed far beyond the $I_{\max}$ values calculated above.

In the present work we assume axial symmetry in the PRM calculations, which according to the CNS calculations (Fig. 7) should be reasonable for all states with the exception of the highest spin states for the bands having just one high-j proton. In the triaxial case the dimensions grow rapidly because each basis state can be combined with several K values, which makes calculations time consuming. We also assume that the effect of the pairing interaction is negligible, which is supported by the fact that in the high-spin regime we consider, the moments of inertia are well described in unpaired calculations (see Fig. 6 and Fig. 10 below and also Ref. [5]).

B. The $(h_{9/2})^2$ configuration

Figure 9 compares CNS calculations with the result of the PRM in the case of two $h_{9/2}$ protons coupled to our neutron configuration. The deformation trajectory of this configuration falls close to the the one for the $\pi(i_{13/2}h_{9/2})$ configuration in Fig. 7. The lowest band in the CNS calculations is obtained when placing the two protons in opposite signatures, thus coupling their spin in opposite directions and a corresponding band is lowest also in the PRM calculations. This is contrary to the case with the two protons in different shells (see Fig. 4) where the parallel coupling was favored in the PRM calculations. The yrast $\pi(h_{9/2})^2$ band splits into two at low spins which is due to the signature splitting of the highest $i_{13/2}$ neutron level. The antiparallel coupling of the two protons produces no large $B(M1)$ values. To obtain a band with large $B(M1)$ values the protons have to align their spin vectors. In the CNS model, this can be achieved by exciting one of them within the $h_{9/2}$ shell so that both are in orbitals of the same signature. As seen in the top panel of Fig. 9 this produces a $\Delta I = 1$ band labeled A at a higher energy. In the PRM calculation shown in the lower panel this excitation energy is reduced making this band close to the lowest one when approaching $I = 30$. Because this magnetic band is not the lowest $(h_{9/2})^2$ band it may be more difficult to observe than magnetic bands formed with the two protons in different shells or with only one high-j proton. At $I = 31.5$ $M1$ transitions within the magnetic band are calculated to be of similar strength as $M1$ transitions connecting it with the lower band. Approaching lower spins the strength of transitions between the bands decreases rapidly. At higher spins (around $I = 30$) the results obtained from the CNS model agree quite well with the PRM. This is to be expected since with increasing spin the orientation of the total angular momentum is driven into the direction perpendicular to the symmetry axis where the PAC descriptions should work well.

In the PRM, spin projections on any axis is always zero. Therefore, to compare the spin orientation, expectation values

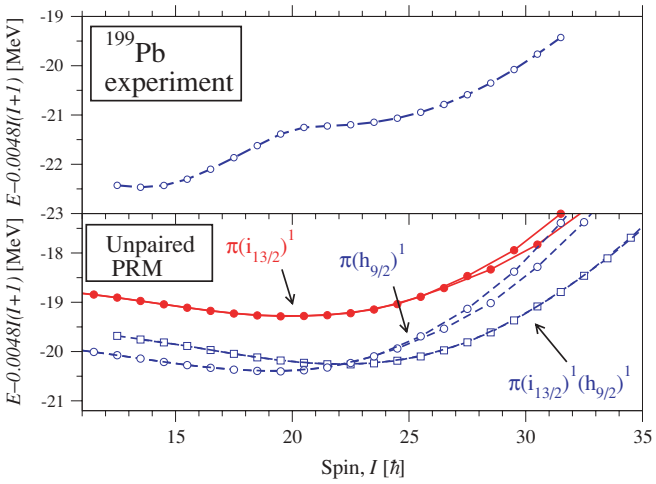

FIG. 10. (Color online) Calculated rotational bands in ^{199}Pb together with experiment. The experimental data is taken from [2,27] where this band is labeled band 1. There is an additional high-spin band observed in this nucleus which has not yet been linked to the low-spin structures.

of the squares of the spin projection operators are calculated. The results for the $(h_{9/2})^2$ bands are illustrated in the right panels of Fig. 9. At spin $I = 20.5$, the magnetic band labeled A has a large proton spin projection on the symmetry axis, which makes the total spin vector tilt toward the symmetry axis. The total spin increases due to the alignment of the protons with the collective spin component and also because of an increase in collective spin. At spin 30.5 the collective spin vector contributes with approximately 10 units for both bands.

C. PRM description and comparison with experiments

Figure 10 shows calculated configurations of ^{199}Pb compared with experiments [27]. The total energy for each configuration and spin has been minimized with respect to ε_2 deformation using a mesh consisting of six different values ($\varepsilon_2 = \{-0.06, -0.08, -0.10, -0.12, -0.14, -0.16\}$). For the larger deformations the fit used to extract the moment of inertia for the core could be done with a good accuracy with a maximum discrepancies for any point less than 0.05 MeV. For smaller deformations the core becomes less collective and a smooth fit becomes more difficult. The biggest discrepancies, which are about 0.2 MeV for some points, are found for the smallest deformation. All configurations have the same neutron configuration.

The valence neutrons are treated as 11 particles in a deformed $(i_{13/2})$ shell. The valence protons are also confined to different deformed high-j shells. In the cases where there is a single hole in the $N = 4$ shell the valence space for the hole is taken to be the entire $N = 4$ shell with the exception of orbits of $g_{9/2}$ character. The total energy calculated using different valence spaces is shown in Tables I and II. At the small deformations considered, the j shells are not so mixed and the strongest couplings of $H_{\rm rot}$ occur between orbitals originating from the same deformed j shell. Therefore, increasing the valence space much beyond the single deformed j shells is found to have a small effect on the energy.

TABLE I. Effects of truncation of basis states on the energy levels of ^{199}Pb. The energies for the $\pi(i_{13/2})^1(h_{9/2})^1\upsilon(i_{13/2})^{-3}$ configuration at spin 20.5 and 30.5 is indicated as a function of the number of basis states used for the $i_{13/2}$ proton. The deformation is kept fixed at $\varepsilon_2 = -0.14$. The number of basis states for the $h_{9/2}$ proton is fixed at 12 and the for the neutron holes, the 256 lowest excitations within the deformed $i_{13/2}$ shell is used as a basis.

Number of basis states	$E(20.5)$	$E(30.5)$
4	−18.236	−14.353
6	−18.255	−14.574
10	−18.258	−14.684
14	−18.258	−14.697
16	−18.258	−14.698
18	−18.258	−14.698
24	−18.258	−14.699
30	−18.258	−14.699

The $\pi(i_{13/2})^1(h_{9/2})^1$ configuration has been suggested for the experimental band on the basis of TAC calculations [28]. This assignment is consistent with the fact that the lowest state observed has $I = 25/2$, which coincides with the band head spin obtained from the parallel coupling of the two high-j protons and the odd $i_{13/2}$ $\Omega = 3/2$ neutron. This is also the dominating component (≈40%) in the calculated wavefunction. However, this amplitude might change if pairing was included in the model.

Comparing energies in Fig. 10, all bands have similar slopes as the experimental band after the backbending around spin 20. The bands with just one high-j proton develop a signature splitting at the highest spins that is not seen in the experimental band. However, when performing CNS calculations for the $\pi(i_{13/2})^1$ band we found that this signature splitting is reduced when triaxial deformations are allowed. Figure 11 compares calculated transition energies for the $\pi(i_{13/2})^1(h_{9/2})^1$ and the $\pi(i_{13/2})^1$ configurations with the experimental ones. As seen from this figure there is no sign of signature splitting in the experimental data.

Figure 12 shows the calculated and observed [26] $B(M1)$ values for in-band transitions. The $B(M1)$ values increase with the number of particles having a angular momentum pointing in the direction of the symmetry axis and decrease as the

TABLE II. Same as in Table I but as a function of the number of basis states used for the $h_{9/2}$ proton while the number of basis states for the $i_{13/2}$ proton is fixed at 14.

Number of basis states	$E(20.5)$	$E(30.5)$
4	−18.231	−14.468
6	−18.249	−14.540
10	−18.258	−14.689
12	−18.258	−14.697
16	−18.258	−14.698
18	−18.258	−14.698
22	−18.258	−14.702
28	−18.258	−14.702
30	−18.258	−14.702

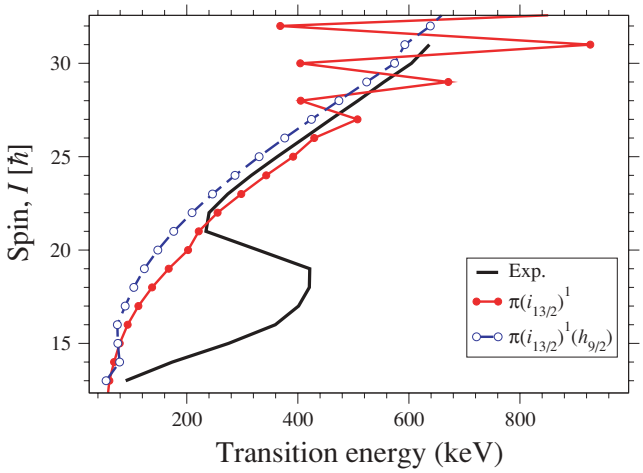

FIG. 11. (Color online) The calculated $\pi(i_{13/2})^1(h_{9/2})^1$ and $\pi(i_{13/2})^1$ configurations of ^{199}Pb compared with the experimental band 1 in a spin versus transition energy plot.

proton and neutron angular momenta align. The calculated $B(M1)$ values for the $\pi(i_{13/2})^1(h_{9/2})^1$ configuration are larger than the ones obtained using the TAC model [26,28]. Close to spin 20, TAC gives $B(M1) \approx 9\mu_N^2$, whereas the PRM gives $B(M1) = 10.8\mu_N^2$ at spin 20.5. At higher spin the differences increase. For example at spin 27.5 the PRM gives $B(M1) = 7.7\mu_N^2$, whereas TAC predicts $B(M1) \approx 4\mu_N^2$. Small differences can be expected and may be a result of the different models. One difference is that a constant deformation of $\varepsilon_2 = -0.1$ is used in the TAC calculation, whereas we obtain $\varepsilon_2 \approx -0.14$. However, the sharper decrease with angular momentum obtained in the TAC model is an indication that there may be differences in the alignment process.

The best agreement with experiment for the $B(M1)$ values is obtained for the band with just one $i_{13/2}$ proton that has positive parity. The experimental band has been suggested to have negative parity but the parity is not determined experimentally [2].

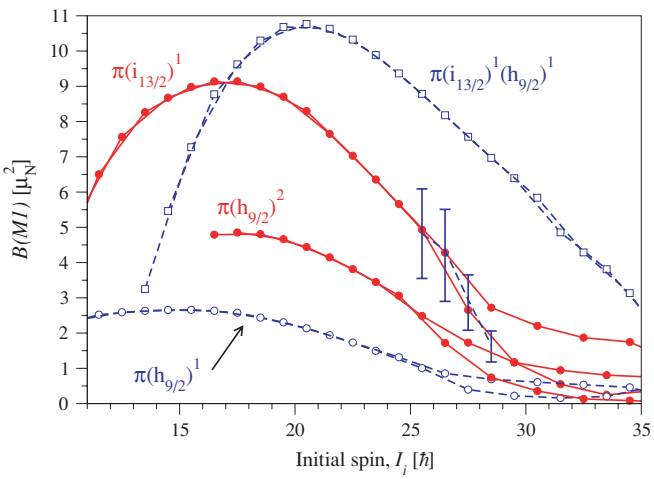

FIG. 12. (Color online) $B(M1)$ values for the calculated bands in ^{199}Pb and comparison with experimental values [26].

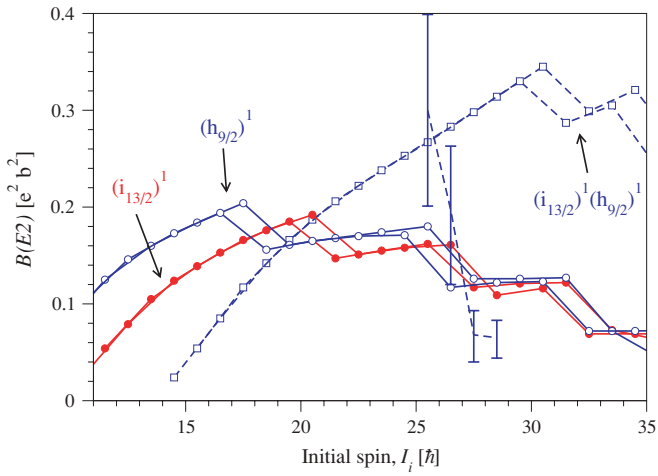

FIG. 13. (Color online) Calculated $B(E2)$ values for the ^{199}Pb configurations in Fig. 10 compared with observed values [26]. Deformation changes in steps of $\Delta\varepsilon_2 = 0.02$ causes the staggering seen in the theoretical curves that probably would become smoother if more deformation points were used when minimizing the total energy. The approximation that the initial and final states have the same deformation, corresponding to the deformation of the initial state, is made when calculating $B(E2)$ and $B(M1)$ values.

Figure 13 shows the calculated and observed [26] $B(E2)$ values. The experimental values show a rapid decrease toward the highest spins observed. A similar decrease is seen for the configurations having just one high-j proton, which is due to the decrease of the quadrupole deformation with increasing angular momentum. According to the CNS calculations these configurations become triaxial at the highest spins observed, which leads to a substantial reduction of the $B(E2)$ values. Thus one might expect a larger decrease and thus a closer correspondence with experiment if triaxiality was taken into account in the calculation. The $\pi(i_{13/2})^1(h_{9/2})^1$ configuration is calculated to be more collective than the other configurations and does not show the rapid decrease, which leads to large discrepancies with experiment at the highest spins.

To investigate whether the sharp decrease of the experimental $B(M1)$ values could be reproduced using the assigned $\pi(i_{13/2})^1(h_{9/2})^1$ configuration, and with a reasonable adjustment of the model parameters, we compare different calculations in Fig. 14. The curve denoted by A is obtained for a constant deformation of $\varepsilon_2 = -0.14$, which is the self-consistent value obtained by minimizing the energy with respect to quadrupole deformation for spin values $I \lesssim 30$. By reducing the deformation substantially to $\varepsilon_2 = -0.06$ the protons become less strongly coupled to the symmetry axis and align more with the total spin vector which reduces the $B(M1)$ values at the higher spins as seen for case B. Note that in the previous TAC calculations for these bands [2,28] using the theoretical model described in Ref. [29] the deformation is largely treated as a free parameter in the sense that the quadrupole coupling parameter is fitted to reproduce experimental deformations. With a deformation of $\varepsilon_2 = -0.06$ the $B(M1)$ values can be further reduced by decreasing the moment of inertia for the core by 30% as seen in case C.

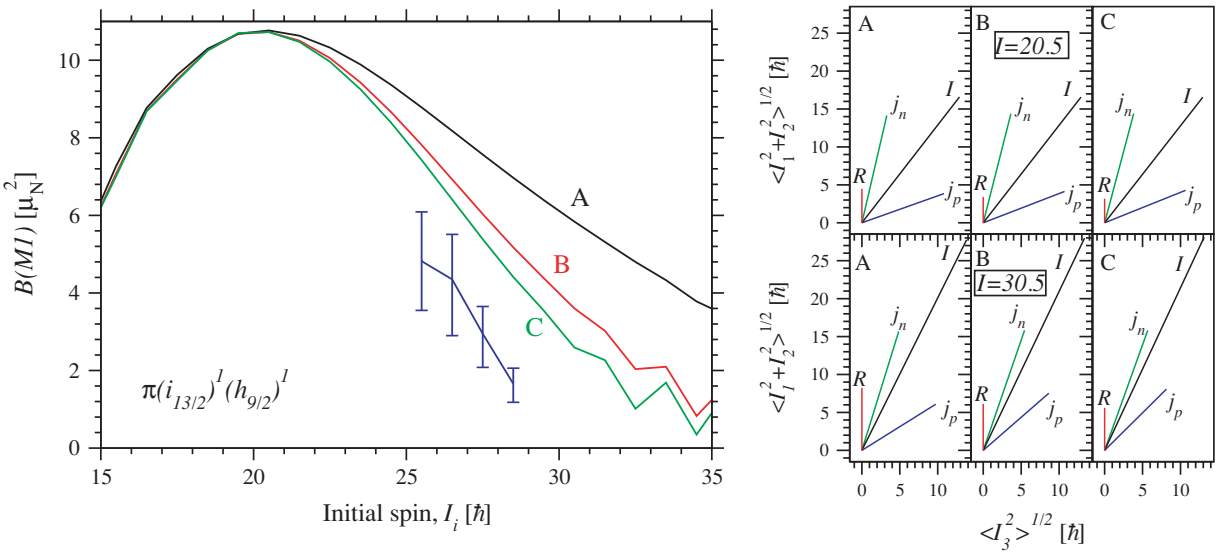

FIG. 14. (Color online) $B(M1)$ transitions for the $\pi(i_{13/2})^1(h_{9/2})^1$ configuration of ^{199}Pb. The curve denoted A is obtained using a constant deformation of $\epsilon_2 = -0.14$. For curve B a much smaller deformation of $\epsilon_2 = -0.06$ is used. For curve C, $\epsilon_2 = -0.06$ and the core moment of inertia has been lowered with 30% with respect to case B. Experimental values for band 1 are shown with error bars. In the panels to the right the spin orientation in the three cases, A, B, and C, is illustrated for $I = 20.5$ and $I = 30.5$.

A decrease of the moment of inertia could be achieved for example if the $h_{9/2}$ subshell was lowered so that the neutron core was essentially confined to the low-j $f_{5/2}$, $p_{3/2}$, and $p_{1/2}$ subshells, see Fig. 8. However, as seen in in Fig. 14 the resulting change in the $B(M1)$ values is pretty small, indicating that the results are not so sensitive to the moment of inertia used for the rotor.

The calculated $B(M1)$ values depend mainly on the geometry of the spin vectors as illustrated in the right panel of Fig. 14. At spin 20.5 the different parameter choices A, B, and C predict almost the same spin orientations being reflected in the almost identical $B(M1)$ values. At spin 30.5, differences in the alignment occur for the different parameter choices. A smaller moment of inertia for the core makes it favorable to build more spin by aligning the neutron and proton spin vectors. The amount of core spin obtained at spin 30.5 for $\varepsilon_2 = -0.14$ is roughly $\sqrt{\langle R^2\rangle} = 8$ units, which is a reasonable value considering the $I_{\max}$ values discussed above. In our calculations the core spin is always constrained to point in the direction perpendicular to the symmetry axis. Thus at higher spins we tend to get a situation where the proton spin is forced to point in the direction of the rotor spin. If this constraint was dropped it is possible that the core spin would tilt toward the symmetry axis, which could lead to a decrease of both the $B(M1)$ and the $B(E2)$ values. This situation may then be more in agreement with results obtained from TAC calculations where an almost constant tilting angle is calculated [2].

V. THE TILTING OF THE NEUTRON SPIN VECTORS

For the magnetic bands the anisotropy of the distribution of the proton angular momentum projections on the symmetry axis k_p causes a division of the total wave function into two uncoupled parts. This is easy to realize because in the axially symmetric case couplings only occur between basis states differing by $\Delta k_p \leqslant \pm 1$. Thus if the wave function can be divided into two parts with positive and negative k_p values, respectively, which are separated by $\Delta k_p > \pm 1$, these parts will not couple.

In this case the total wave function can be written as $|\Psi^I\rangle = \frac{1}{\sqrt{2}}(|\Phi_+\rangle + |\Phi_-\rangle)$, where the signs indicate that $|\Phi_+\rangle$ and $|\Phi_-\rangle$ contain only positive or only negative values of k_p, respectively. Explicitly the $|\Phi_+\rangle$ wave function can be written

$$|\Phi_+\rangle = \sum_{\alpha,k_p>0} a_\alpha N_{\alpha K}\sqrt{\frac{2I+1}{16\pi^2}}|IMK\rangle|\alpha k_p k_n\rangle + \sum_{\alpha,k_p<0} b_\alpha N_{\alpha K}\sqrt{\frac{2I+1}{16\pi^2}}(-1)^{I-K}|IM-K\rangle e^{-ij_2\pi} \times |\alpha k_p k_n\rangle,$$

with an analogous expression for $|\Phi_-\rangle$. These wave functions are related through the operation $|\Phi_-\rangle = e^{-ij_2\pi}e^{iI_2\pi}|\Phi_+\rangle$. Because $|\Psi^I\rangle$ is an eigenstate of the Hamilton operator, $H\frac{1}{\sqrt{2}}(|\Phi_+\rangle + |\Phi_-\rangle) = \frac{1}{\sqrt{2}}E(|\Phi_+\rangle + |\Phi_-\rangle)$. If the anisotropy is sufficiently large $H|\Phi_+\rangle$ and $H|\Phi_-\rangle$ can be expanded in states having only positive respectively negative values of k_p. In this case, the eigenvalue relation separates into two uncoupled equations $H\frac{1}{\sqrt{2}}|\Phi_\pm\rangle = \frac{1}{\sqrt{2}}E|\Phi_\pm\rangle$, showing that $|\Phi_\pm\rangle$ are also eigenstates of the Hamiltonian with the same eigenvalue. The $\frac{1}{\sqrt{2}}(|\Phi_+\rangle - |\Phi_-\rangle)$ wave function can be expanded in basis states of "wrong signature," i.e., basis states that combines the two terms in Eq. (2) with the wrong sign. Thus if the two solutions $|\Phi_\pm\rangle$ are degenerate the $|\Phi_+\rangle$ state can be obtained by solving the PRM within the basis of "wrong signature" and then adding this solution to the normal solution. This method was used in Ref. [30], where the case of two particles coupled to a rotor was studied and compared with TAC results. Even in cases when the wave function does

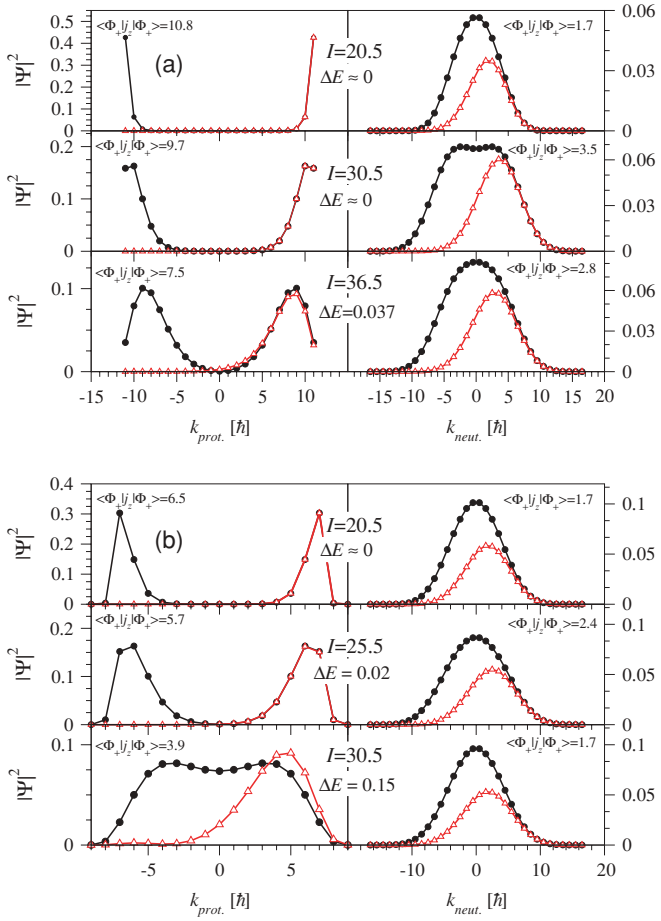

FIG. 15. (Color online) Panel (a) shows calculated k_p- and k_n-distributions for the $\pi(i_{13/2})^1(h_{9/2})^1\nu(i_{13/2})^{-3}$ configuration of ^{199}Pb at a constant deformation of $\varepsilon_2 = -0.14$. The same distribution is illustrated in panel (b) for the $\pi(i_{13/2})^1(N=4)^{-1}\nu(i_{13/2})^{-3}$ configuration at a constant deformation of $\varepsilon_2 = -0.10$. ΔE indicates the calculated energy difference in MeV between the two wave functions with the correct and the "wrong" signature. If the deformation is reduced substantially ($\varepsilon_2 = -0.06$) the $\pi(i_{13/2})^1(h_{9/2})^1\nu(i_{13/2})^{-3}$ configuration obtains a slightly larger maximum asymmetry in the neutron distribution, ($\langle\Psi_+|j_z^\nu|\Psi_+\rangle = 4.1$ at $I = 28.5$).

not not split up in components with positive and negative k_p values, we will define $|\Phi_+\rangle$ using the same procedure.

The wave function $|\Phi_+\rangle$ is illustrated for two of our calculated bands in Fig. 15. This figure shows the probability distributions with respect to k_p both for $|\Psi^I\rangle$ and $|\Phi_+\rangle/\sqrt{2}$ for different I values and the corresponding distribution for the neutrons. For the $\pi(i_{13/2})^1(h_{9/2})^1\nu(i_{13/2})^{-3}$ configuration in panel (a) of Fig. 15 it is seen how the protons gradually tilt away from the symmetry axis toward the neutrons. The neutrons obtain a maximum asymmetry at spin 30.5, where $\langle\Psi_+|j_z^\nu|\Psi_+\rangle = 3.5$, but this value becomes smaller when the total angular momentum increases. At $I = 30.5$ the total $\langle\Psi_+|j_z|\Psi_+\rangle$-value is 13.2, which is larger than the maximum projection obtained for the protons alone. Thus these calculations are consistent with the predictions of the shears mode [3] in the sense that total angular momentum is formed not by an alignment of the proton spin vector along

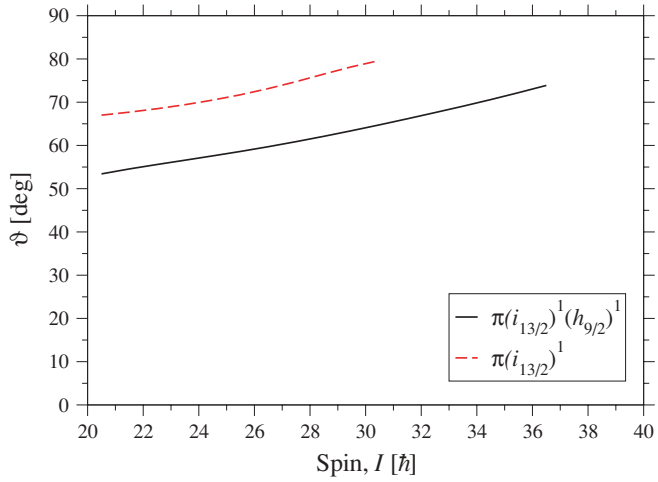

FIG. 16. (Color online) Tilt angle as a function of spin for the ^{199}Pb configurations in Fig. 15. The tilt angle is obtained as $\arccos[\langle\phi_+|j_z|\phi_+\rangle/\sqrt{I(I+1)}]$.

the perpendicular direction but rather by the simultaneous alignment of the proton and neutron spin vectors along the total spin vector. The angle the total spin vector makes with the symmetry axis is shown in Fig. 16. In the TAC calculations, this angle is essentially independent of spin. The angle calculated in the PRM for the $\pi(i_{13/2})^1(h_{9/2})^1$ configuration increases somewhat from $\vartheta = 53^\circ$ at spin 20.5 to $\vartheta = 66^\circ$ at spin 31. This increase is most likely caused by the increase in rotor spin (compare Fig. 14).

The k distributions for the $\pi(i_{13/2})^1(N=4)^{-1}\nu(i_{13/2})^{-3}$ configuration is shown in panel (b) of Fig. 15. In this case the asymmetry caused by the single $i_{13/2}$ proton is not enough to generate a splitting of the wave function at the highest spins. Thus although the k_p distribution still shows two bumps for positive and negative k_p values at $I = 30.5$, the two branches are no longer uncoupled. The corresponding tilt angle is illustrated in Fig. 16.

In our numerical calculations we found that diagonalizing the PRM Hamiltonian in the basis with the wrong signature gives eigenstates that interpolates the $\ldots, I, I+2, \ldots$ states to the $\ldots, I+1, I+3, \ldots$ states in a smooth way. The energy difference between the interpolated solution with the wrong signature and the ones with the correct signature at a certain spin can then be taken as a measure of the signature splitting. When these two solutions are degenerate, it implies that the wave function can be separated into two uncoupled branches. In panel (b) of Fig. 15 it is seen how couplings may appear in the high spin regime when the K value is reduced. These couplings breaks the degeneracy and a signature splitting appears at higher spins in Fig. 10 for the corresponding configuration. It is also interesting to notice that the above scenario is not restricted to bands having large K projections. For example, it is possible to have two protons of different parity coupled to $K \sim 0$ and neutrons with angular momenta pointing on a perpendicular axis. If the k_p values of the individual protons are sufficiently large they will generate an asymmetry giving rise to solutions $|\Phi_\pm\rangle$ and a vanishing signature splitting. Thus also in this case with $K \sim 0$ one

would expect regular $\Delta I = 1$ sequences as exemplified for bands with the antiparallel coupling of the two protons seen in Fig. 4. If the two protons are in the same shell and coupled to $K \sim 0$ no such division can be made and one thus expects regular $\Delta I = 2$ sequences as seen for the lowest band in Fig. 9.

VI. CONCLUSIONS AND DISCUSSIONS

A particle+rotor model (PRM) has been developed where several particles are coupled to a rotating core. The core is described as a triaxial rotor while the basis space for the particles are the orbitals of a deformed single-particle potential. The limit of the number of particles that can be treated explicitly is determined by the dimensions of the matrices that are set up and diagonalized. The core parameters are determined from cranking calculations. Although this is straightforward in the axial case, it becomes questionable how to extract three moments of inertia in a consistent way for triaxial nuclei. For this reason and also because of the large matrix dimensions in the triaxial case, we have confined ourselves to axial nuclei in this first application. In principle, it would be as straightforward to consider quasiparticles rather than particles but the division between the particle space and the core space would be less transparent. Therefore, and because we are mainly interested in high-spin states, pairing is not included in the present applications.

The formalism has been applied to describe the magnetic bands in the lead region. It turns out that the core parameters become very different depending on the core space but the final results become similar for different divisions of valence and core spaces. There are, however, important differences that can be understood mainly from the freedom given to the particles to tilt away from the cranking direction. In the magnetic bands in lead nuclei, it is evident that the spin vectors of the high-K protons start out as pointing along the symmetry axis and only slowly gets more aligned along the perpendicular cranking direction. However, the tendency for the spin vectors of the high-j neutron holes to tilt toward the symmetry axis can be accounted for only if they are included in the particle space. Although this tilting appears to have only small effects on the energies, it is much more important for the transition probabilities. The final result appears to be a shears effect where the tilting angle of the total spin vector is relatively constant in a large spin interval.

The feature of the PRM to treat some particles explicitely while other particles are only included as building blocks of a core is clearly somewhat artificial. This is not the case for the TAC model, which thus has some advantages compared with the present PRM calculations. However, the fact that the most important single-particle angular momenta are considered explicitely and coupled according to the laws of quantum mechanics in the PRM model is often important or even crucial. For example, while the TAC model assumes signature degeneracy, the splitting of the two signatures is calculated in a consistent way in the PRM model. Thus, it is possible to follow how the two signatures of some magnetic bands might slowly split apart when the bands come close to their maximum spin values, corresponding to a transition from a tilted solution to a PAC solution. This appears especially important for calculated bands with only one high-j proton that have not been considered previously. A transparent understanding of this splitting and the underlying coupling between different basis states is obtained by considering the K distribution of the wave functions.

Another important special case is with both of the high-j protons in the same high-j orbital. It then turns out that the magnetic band is not lowest in energy that put doubts on some of the assignments for observed bands in, e.g., ^{196}Pb. Although we cannot make any firm new configuration assignments in ^{199}Pb the (to our knowledge) first comparison of calculated $B(E2)$ values with experiments presented here gives new insight into the configurations of the bands. The experimental $B(E2)$ values decrease toward the highest observed spins as would be expected for a terminating band. However, our calculations suggest that the usual interpretation with configurations having two high-j protons are too collective to terminate at these spins. We also demonstrate that less collective configurations with only one high-j proton gives a better agreement with the experimental $B(E2)$ values. However, to make any firm assignments one would have to make a more extensive study and consider more data from several isotopes. More data on transition probabilities in the high-spin regime where all high-j angular momenta are essentially aligned would be especially valuable.

In addition to the applications on magnetic bands exemplified above, it should be possible to apply the present many-particles–plus–rotor formalism to describe other high-spin phenomena such as the wobbling motion and chiral rotation or to get a better understanding of the relative properties of superdeformed bands. The model enables an intuitive description of the coupling of the particle angular momenta in different kinds of rotational bands.

ACKNOWLEDGMENT

The authors thank Herbert Hübel for useful discussions. This work was supported by the Swedish Science Research Council.

APPENDIX A

The expression for rotated creation operators may be obtained using Schwinger's oscillator model of angular momentum. The derivation below uses results from chapter 3.8 of Ref. [31].

$$
\begin{aligned}
& e^{-ij_2\pi} a^\dagger_{j\Omega} e^{ij_2\pi} \\
&= e^{-ij_2\pi} \frac{\left(a^\dagger_+\right)^{j+\Omega}\left(a^\dagger_-\right)^{j-\Omega}}{\sqrt{(j+\Omega)!(j-\Omega)!}} e^{ij_2\pi} \\
&= \frac{[e^{-ij_2\pi} a^\dagger_+ e^{ij_2\pi}]^{j+\Omega}[e^{-ij_2\pi} a^\dagger_- e^{ij_2\pi}]^{j-\Omega}}{\sqrt{(j+\Omega)!(j-\Omega)!}} \\
&= \frac{\left[a^\dagger_+ \cos\left(\frac{\pi}{2}\right) + a^\dagger_- \sin\left(\frac{\pi}{2}\right)\right]^{j+\Omega}\left[a^\dagger_- \cos\left(\frac{\pi}{2}\right) - a^\dagger_+ \sin\left(\frac{\pi}{2}\right)\right]^{j-\Omega}}{\sqrt{(j+\Omega)!(j-\Omega)!}} \\
&= \frac{\left[a^\dagger_-\right]^{j+\Omega}\left[-a^\dagger_+\right]^{j-\Omega}}{\sqrt{(j+\Omega)!(j-\Omega)!}} = (-1)^{j-\Omega} a^\dagger_{j-\Omega}
\end{aligned}
$$

This phase factor differs with a sign from the one in [9] since the rotation is performed in the opposite direction.

APPENDIX B

As an example on how to evaluate matrix elements between our basis states we take the j_3^2 operator. This operator acting between two of our basis states may be written

$$\left\langle \Psi^I_{MK'\alpha'} \middle| j_3^2 \middle| \Psi^I_{MK\alpha} \right\rangle = N'N\big[\delta_{K',K}\langle\alpha'|j_3^2|\alpha\rangle + (-1)^{I-K}\delta_{K',-K} \times \langle\alpha'|j_3^2|\widetilde{\alpha}\rangle\big],$$

where we have used the relation $e^{ij_2\pi}e^{-iI_2\pi}j_3^2e^{iI_2\pi}e^{-ij_2\pi} = j_3^2$. The total Hamiltonian $H_{\rm rot}$ can be divided into groups of operators that fulfill $e^{j_2\pi}e^{-I_2\pi}Fe^{I_2\pi}e^{-j_2\pi} = F$ (see Ref. [9] for details). The j_3^2 operator itself may be expressed as a sum over one- and two-body operators

$$\begin{aligned} j_3^2 &= \sum_{i,j,k,l}\langle i|j_3|j\rangle a_i^+a_j\langle k|j_3|l\rangle a_k^+a_l \\ &= \sum_{i,j,k,l}\langle i|j_3|j\rangle\langle k|j_3|l\rangle a_i^+a_ja_k^+a_l \\ &= \sum_{i,l}\langle i|j_3^2|l\rangle a_i^+a_l - 2\sum_{i<k,l<j}(\langle i|j_3|j\rangle\langle k|j_3|l\rangle \\ &\quad - \langle k|j_3|j\rangle\,\langle i|j_3|l\rangle)a_i^+a_k^+a_ja_l. \end{aligned}$$

This form with a restricted summation is convenient when calculating matrix elements (for details see [32]). The same procedure as outlined here can be used for all matrix elements of $H_{\rm rot}$. Reference [12] describes how to evaluate the single-particle matrix elements when using a basis of stretched harmonic oscillator wave functions, which is the basis used in our numerical calculations.

[1] S. Frauendorf, Rev. Mod. Phys. **73**, 462 (2001).
[2] H. Hübel, Prog. Part. Nucl. Phys. **54**, 1 (2005).
[3] G. Baldsiefen *et al*., Nucl. Phys. **A574**, 521 (1994).
[4] A. V. Afanasjev, D. B. Fossan, G. J. Lane, and I. Ragnarsson, Phys. Rep. **322**, 1 (1999).
[5] I. Ragnarsson, in *Proceedings of the International Conference on The Nucleus: New Physics for the New Millenium, NAC, Faure, South Africa*, edited by F. D. Smit, R. Lindsay, and S. V. Förtsch (Kluwer Academic/Plenum, New York, 1999), p. 347.
[6] J. J. Valiente-Dobón *et al*., Phys. Rev. Lett. **95**, 232501 (2005).
[7] S. Frauendorf and T. Bengtsson, in *Proceedings of the Symposium on Future Directions in Nuclear Physics with 4π-Gamma Detection Systems of the New Generation, Strasbourg 1991*, edited by J. Dudek and B. Haas (AIP Conf. Proc. 259, New York, 1992), p. 223.
[8] S. Frauendorf, Nucl. Phys. **A557**, 259c (1993).
[9] A. Bohr and B. R. Mottelson, *Nuclear Structure Vol. II* (W. A. Benjamin, Inc., New York, 1975).
[10] I. Ragnarsson and P. B. Semmes, Hyp. Int. **43**, 425 (1988).
[11] J. Almberger, I. Hamamoto, and G. Leander, Phys. Scr. **22**, 331 (1980).
[12] S. E. Larsson, G. Leander, and I. Ragnarsson, Nucl. Phys. **A307**, 189 (1978).
[13] T. Bengtsson and I. Ragnarsson, Nucl. Phys. **A436**, 14 (1985).
[14] Z. Szymanski, *Fast Nuclear Rotation* (Oxford University Press, Oxford, 1983).
[15] ARPACK http://www.caam.rice.edu/software/ARPACK/.
[16] K. T. Hecht and G. R. Satchler, Nucl. Phys. **32**, 286 (1962).
[17] H. Toki and A. Faessler, Nucl. Phys. **A253** 231 (1975); A. Faessler, Rep. Prog. Phys. **45**, 653 (1982) .
[18] M. A. J. Mariscotti, G. Scharff-Goldhaber, and B. Buck, Phys. Rev. **178**, 1864 (1969).
[19] N. Rowley and K. F. Pál, in *Proceedings of Symposium on Future Directions in Nuclear Physics with 4π-Gamma Detection Systems of the New Generation, Strasbourg, 1991*, edited by J. Dudek and B. Haas (AIP Conf. Proc. 259, New York, 1992), p. 463.
[20] J. Almberger, I. Hamamoto, and G. Leander, Nucl. Phys. **A333**, 184 (1980).
[21] V. M. Strutinsky, Nucl. Phys. **A95**, 420 (1967).
[22] G. Andersson, S. E. Larsson, G. Leander, P. Möller, S. G. Nilsson, I. Ragnarsson, S. Åberg, R. Bengtsson, J. Dudek, B. Nerlo-Pomorska, K. Pomorski, and Z. Szymański, Nucl. Phys. **A268**, 205 (1976).
[23] B. G. Carlsson and I. Ragnarsson, Phys. Rev. C **74**, 011302(R) (2006).
[24] K. Pomorski and J. Dudek, Phys. Rev. C **67**, 044316 (2003).
[25] A. Görgen *et al*., Nucl. Phys. **A683**, 108 (2001).
[26] R. M. Clark *et al*., Phys. Rev. Lett. **78**, 1868 (1997).
[27] H. Hübel *et al*., Z. Phys. **358**, 237 (1997).
[28] M. Neffgen *et al*., Nucl. Phys. **A595**, 499 (1995).
[29] S. Frauendorf, Nucl. Phys. **A677**, 115 (2000).
[30] S. Frauendorf and J. Meng, Z. Phys. A **356**, 263 (1996).
[31] J. J. Sakurai, *Modern Quantum Mechanics* (Addison-Wesley Publishing Company, Inc., Reading, Massachusetts, 1994).
[32] A. Bohr and B. R. Mottelson *Nuclear Structure Vol. I* (W. A. Benjamin Inc., New York, 1969), Appendix 2A.